DISCUSSION BETWEEN A RESERVOIR ENGINEER AND A GEOLOGIST: PERMEABILITY IDENTIFICATION FROM COMPLETION TEST DATA AND BOREHOLE IMAGE LOGS INTEGRATION

Massiot, C.[1], McLean, K.[2], McNamara, D.D.[3], Sepulveda, F.[2], Milicich, S.D.[1]

[1]GNS Science, 1 Fairway Drive, Avalon, Lower Hutt 5010

[2] Contact Energy Ltd.

[3] University of Ireland, Galway, Ireland.

c.massiot@gns.cri.nz

Keywords: *Permeability, Completion test, Borehole image log, Wairakei Geothermal Field.*

ABSTRACT

The location of permeable zones, and preliminary quantification of a geothermal well's production or injection capacity are routinely interpreted from well pressure, temperature, and flow measurements made at different injection rates and during heating after shut-in (also referred to as PTS or completion test data). The spatial resolution of feed zones interpreted from completion test data typically ranges from 10 – 100 m thick. By itself, the completion test dataset cannot inform on the nature of the permeability, i.e. fracture versus formation permeability, and is subject to uncertainties. On the other hand, borehole image logs provide a direct description of the fractures (location, morphology and orientation) and of rock textures intersected by the borehole, to a spatial resolution of ~0.01 – 1 m.

Traditionally, analyses of completion test and borehole image log data are done independently by the reservoir engineer and geologist, respectively. We present a joint interpretation of completion test data and borehole image logs (acoustic and resistivity) from two boreholes in the Wairakei Geothermal Field, New Zealand, highlighting the advantages of a cross-discipline interpretation of a borehole's permeable zones. In the two studied boreholes, we show that feed zones generally correlate with (1) fractures of low acoustic amplitude and visible on the travel-time image of the acoustic image log, and (2) low resistivity fractures with a high resistivity halo on the resistivity image log. In the latter case, fractures with haloes coincide with a reservoir-scale fault modelled independently from 3D modeling of stratigraphic offsets. However, not all fractures of such appearance observed on the image logs correlate with permeable zones. The integrated interpretation of completion test data and image log increases the robustness in the feed zone interpretation (location, extent, fracture or matrix permeability components), and thus can contribute to improving fluid flow numerical models used to sustainably manage geothermal resources.

1. INTRODUCTION

Permeability in volcaniclastic formations is typically controlled by a mixture of fractures and matrix (Grant and Bixley, 2011), with the fracture component generally increasing with depth. Characterising the contribution of both fracture and matrix to permeability is important for field management, and for better understanding of the reservoir for future well siting. This knowledge can guide, for instance, the reservoir modelling decision between a single-porosity (matrix-dominated) and double porosity (fracture-dominated) reservoir model.

Traditional completion testing forms the basis of an interpretation of the permeable depth intervals (feed zones) and their injectivity (contribution to the well flow) in the well. Pressure, temperature, and spinner (PTS) are measured at various water injection rates and during heating-up after injection stops. Drilling losses are also sometimes considered. The feed zones interpreted from completion test data can be subject to uncertainty, which can be due to: 1) presence of downflows which tend to mask any permeable zones at depths below the inflow point (due to constant temperature); 2) balanced well and formation pressures preventing fluid moving from the well into the formation (outflow) or from the formation into the well (inflow); 3) large permeable zones above minor permeable zones, in which case, PTS data may not have enough resolution to detect minor feed zones. Pressure transient analysis is a valuable tool sometimes used during analysis of completion test data, a discussion of which is beyond the scope of this paper.

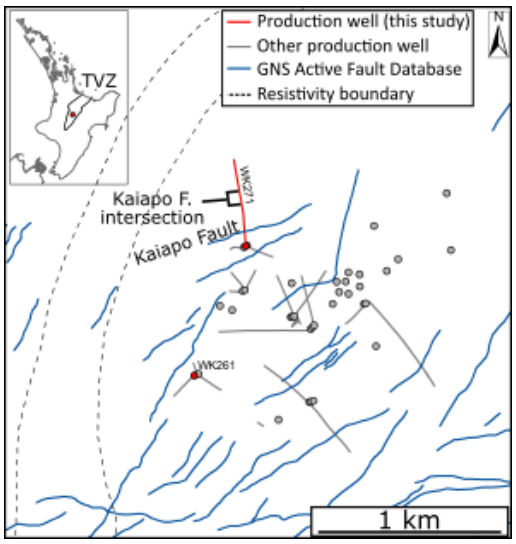

Figure 1: Location map of wells used in this study, nearby wells active faults mapped on surface and the possible Kaiapo Fault intersection with WK271.

Borehole image logs directly image formation textures and fractures intersecting the borehole, and allow fracture location, orientation and apparent thickness measurements. There are two types of borehole image logs: acoustic and resistivity. Interpretation of acoustic image logs acquired with the high-temperature acoustic televiewer ABI85 in >20 boreholes in the Taupo Volcanic Zone (TVZ) since its development in 2009, has provided invaluable observations of the structural and *in-situ* stress settings directly in the reservoirs (Massiot et al., 2013; McNamara et al., 2016 and

references therein). When the borehole can be cooled down <150°C, resistivity image logs (FMI) can be acquired, which has been reported only once before in the TVZ (Halwa et al., 2013).

Fractures identified in borehole image logs are typically 0.01-1 m thick (Massiot et al., 2017), much higher resolution than completion test data which typically ranges from 10-100m thick. Some features are known to be impermeable, such as high acoustic amplitude and high resistivity fractures which are infilled with minerals (Davatzes and Hickman, 2010; Milloy et al., 2015). However, it is not possible to determine if low acoustic amplitude and low resistivity fractures are infilled with minerals or open to fluid flow. It is thus necessary to analyse borehole image logs in combination with completion test data to assess fracture permeability.

McLean and McNamara (2011) considered three boreholes at the Wairakei Geothermal Field for an integrated interpretation of feed zones from completion test data and borehole image logs, illustrating the value of cross-disciplinary geological and reservoir engineering analysis. In this paper, we present a new case study with advanced integrated interpretation of feed zones, image logs and subsurface modelled faults from two boreholes (WK261 and WK271) located in the Te Mihi production zone of the Wairakei Geothermal Field, TVZ (Figure 1) for a more robust interpretation of location, extent, and fracture contribution of permeable zones. We also investigate of the characteristics of permeable fractures in borehole image logs.

2. DATA

Boreholes WK261 and WK271 intersected a volcaniclastic sequence of ignimbrites, tuffs and rhyolites (Figures 2 and 4). The >900-m long image logs span the entire open-hole section. Borehole image logs were processed, quality-checked, and interpreted following the workflow presented in Massiot et al. (2015). All reported depths are with respect to the casing head flange, measured along the boreholes.

WK261 was drilled vertically to a depth of 2059 m, cased to 1144 m. Completion testing (Figures 2 and 3a) with the PTS tool was carried out at three increasing injection rates (57, 114 and 170 t/h) followed by a falloff to zero flow, with various profiles at each injection rate. The fixed tool depth for flow changes was 2052 m.

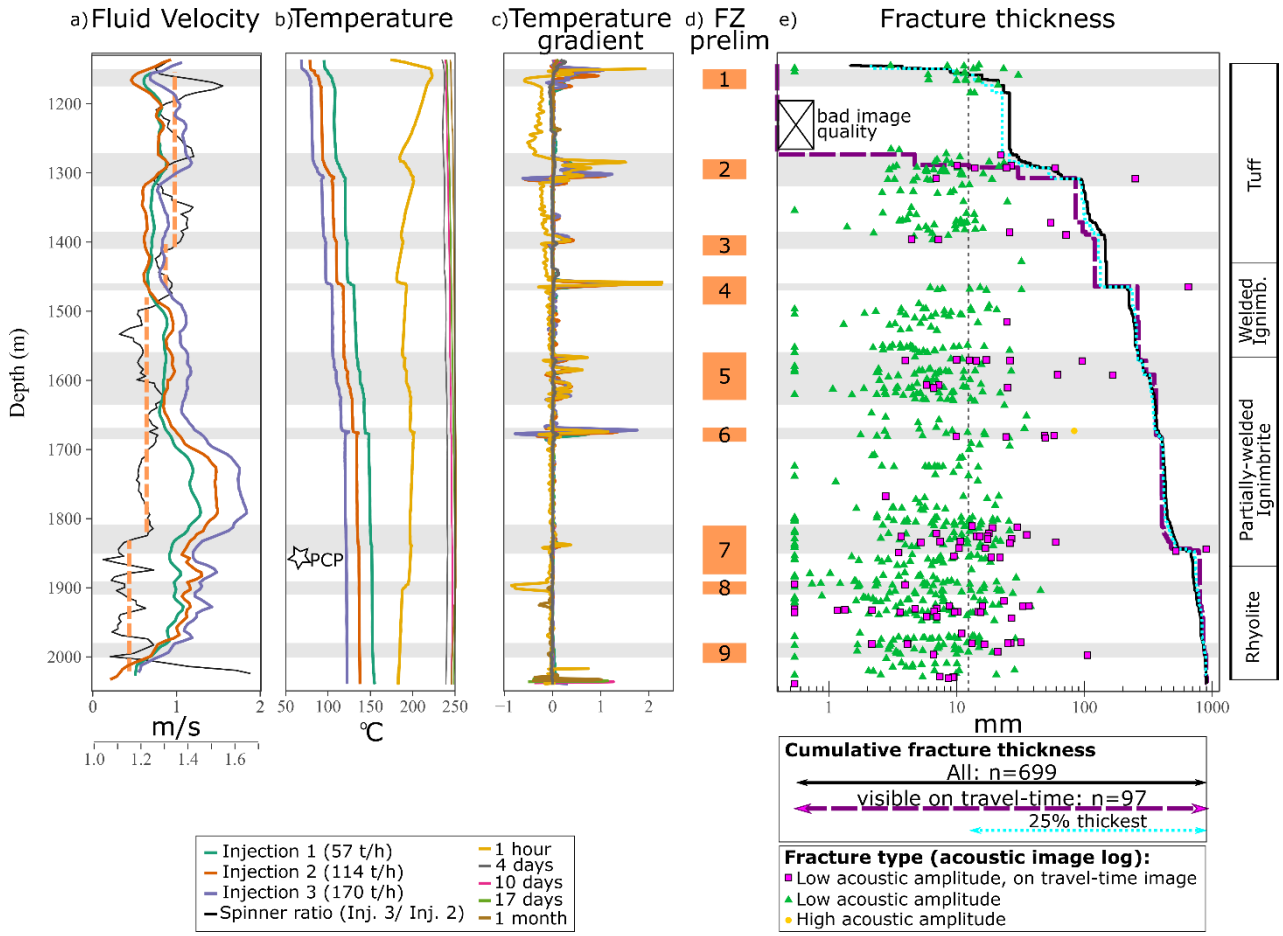

Figure 2: WK261: Completion test and acoustic image log interpretation. (a) Fluid velocity (spinner) at three rates of injection, and spinner ratio (dashed lines: interpreted areas of constant spinner ratio); (b) temperature logs at three injection rates and during heat-up, with the pressure control point (PCP); (c) temperature gradient logs; (d) preliminary feed zone intervals; (e) fracture thickness and morphology, and cumulative fracture thickness of all fractures, fractures of low acoustic amplitude seen on travel-time images and the 25% thickest fractures, plotted on a log-linear scale. The final permeable zone intervals are dashed in grey across all panels.

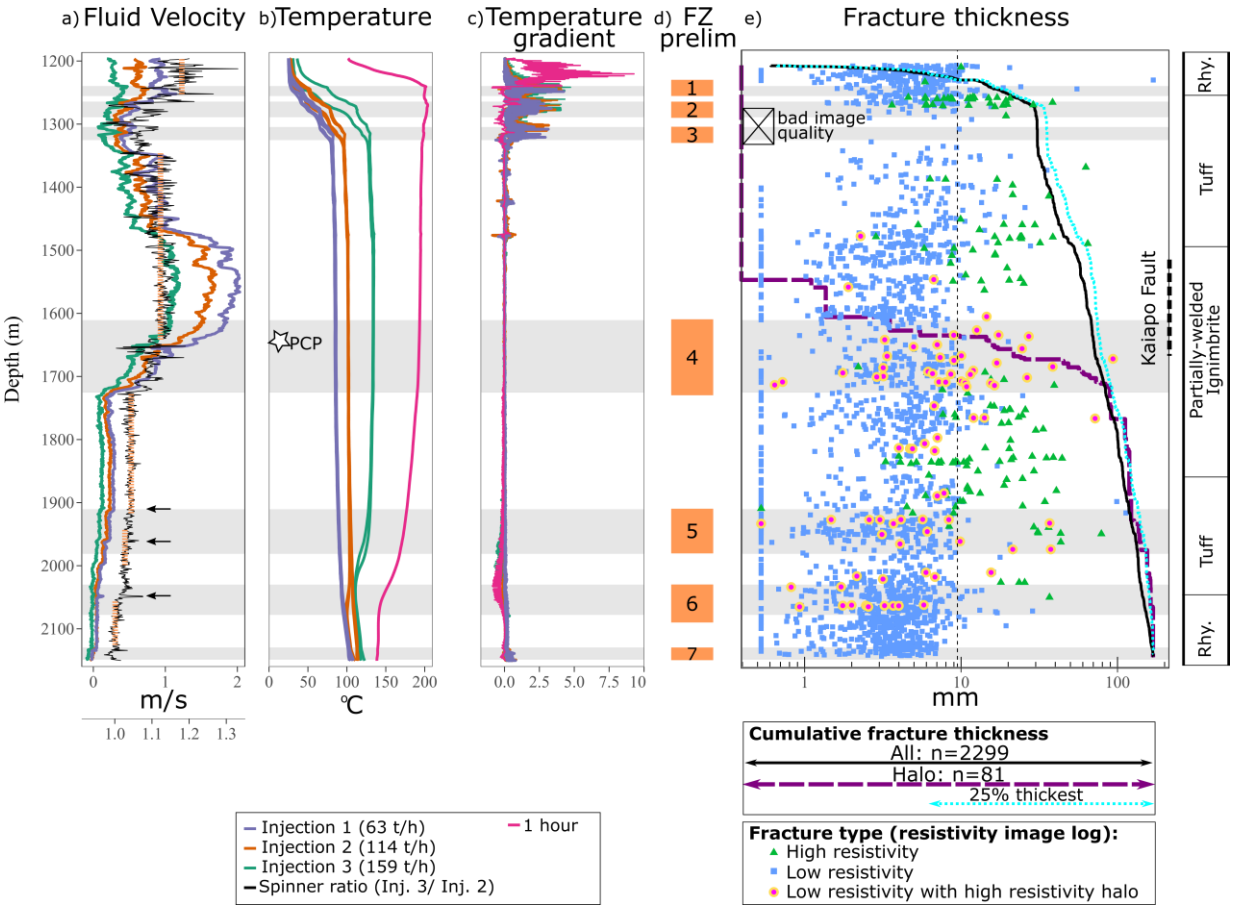

Figure 3: WK271: Completion test and resistivity image log interpretation. Same nomenclature as Figure 1. The intersection between the Kaiapo Fault and the borehole is not precisely constrained.

WK271 was drilled in 2013 to a depth of 2268 m, cased to 1196 m and is deviated ~20° towards NNW (Figure 1). Completion testing (Figure 3 and 4b) with the PTS tool was carried out using three increasing injection rates (63, 114 and 159 t/h) followed by a falloff to zero flow, with various profiles at each injection rate. The fixed tool depth for flow changes was 1120 m, within the casing shoe due to hole stability concerns.

It is of general interest to determine the nature of permeability for permeable wells. The injectivity index (or injectivity, for short) of a well provides a quantitative measure of a well's permeability (e.g. Siega et al., 2014) . Injectivity is routinely obtained from three stable pressures measured at a fixed depth (generally, the depth of the main feed in the well) for three injection rates. WK261 and WK271 have injectivities of 121 and 91 t/h/bar, respectively; Figure 5). In the case of WK271 there is a significant downflow present at all injection rates, which has been accounted for in the injectivity assessment via an enthalpy balance calculation:

$$\dot{m}_3 h_3 = \dot{m}_1 h_1 + \dot{m}_2 h_2$$

where: $\dot{m}$ = mass flow (kg/s), h = enthalpy (kJ/kg) and the numbering refers to locations: 1 = at the wellhead, 2 = the inflow, 3 = total flow below the inflow (injection + inflow combined).

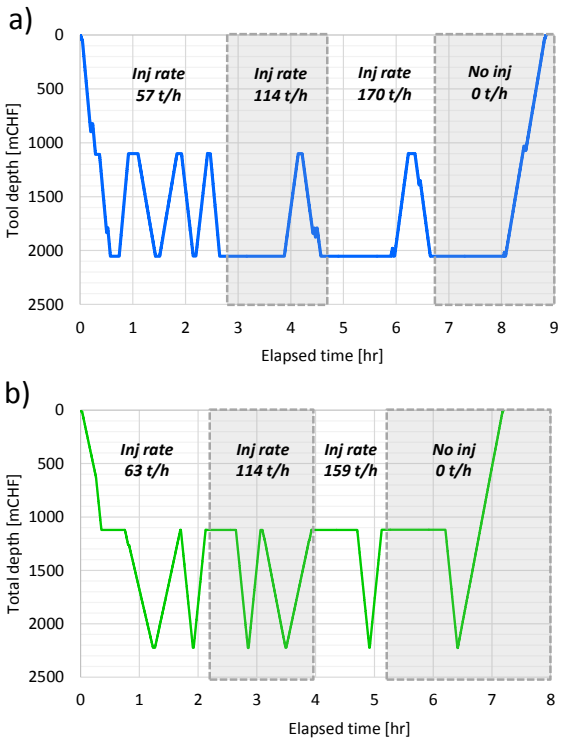

Figure 4: Depth-time charts for PTS tool during completion testing, showing flow rate changes, and profiles run at different speeds, for: a) WK261; b) WK271.

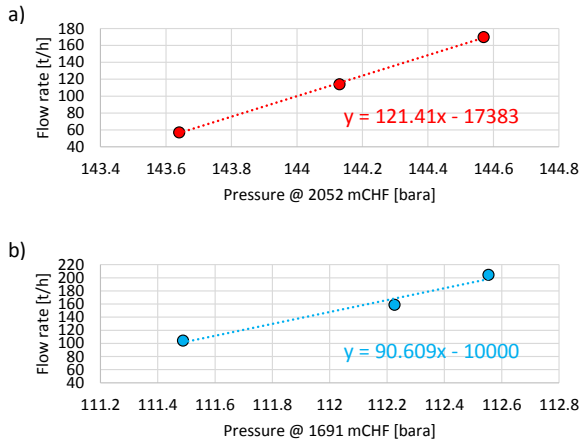

Figure 5: Injectivity charts: a) WK261; b) WK271

3. METHOD

The integrated analysis starts with independent preliminary analysis of completion tests and image logs. Then, both specialists work together and discuss respective interpretations, using them as input into a revised interpretation.

3.1 Completion test data analysis

The preliminary completion test data analysis involves checking the available data for anomalies which could be due to feed zones. Data types used in this study are: 1) changes in temperature gradient during injection; 2) changes in temperature gradient during heatup; 3) fluid velocity profiles from spinner data; 4) ratio of fluid velocity profiles from different injection rates; 5) pressure control point (PCP) during heatup.

3.2 Image log analysis

The image log interpretation is made following the workflow detailed in Massiot et al. (2015). Care was taken to differentiate natural fractures from stress-induced features and layering.

Fractures identified on the acoustic image log (WK261) are separated and plotted into three categories based on their appearance on the image log (Figure 2):

- Fractures of high acoustic amplitude, which are mineralised and cannot conduct fluid flow
- Fractures of low acoustic amplitude, which may be either open to fluid flow or at least partially filled with minerals such as clay, iron oxides, and pyrite (Milloy et al., 2015)
- Fractures of low acoustic amplitude which are seen on the travel-time image. While these fractures may also be filled with clay minerals, they have the highest probability of being open to fluid flow as a topography is observed on the borehole wall

Fractures identified on the resistivity image log (WK271) are separated and plotted into three categories based on their appearance on the image log (Figure 3):

- Fractures of high resistivity, which are likely filled with non-conductive minerals such as quartz or calcite and cannot conduct fluid flow
- Fractures of low resistivity, which may be either open to fluid flow or at least partially filled with minerals such as clay (Halwa et al., 2013)
- Fractures of low resistivity displaying a halo of high resistivity. This high resistivity rim can be caused by the build-up of excess current along the fracture due to materials with unusually high or low conductivity within the fracture (Lofts and Bourke, 1999).

3.3 Discussion between the reservoir engineer and the geologist

The step where both analysts discuss their findings is critical to a robust analysis of the location and extent of permeable zones. The reservoir engineer has a good understanding of the uncertainty of their interpretation, and can look for an observable candidate on the image log justifying the existence of a feed zone. On the other hand, the geologist can propose what constitutes a good contender (either fractures or lithological features) to be permeable, and the reservoir engineer can in turn investigate if there are correlating permeability indicators in the completion test data. Given the uncertainty and sampling rate of completion test data, it is sometimes adequate to extend a permeable zone by a few metres to include a major feature visible on the image logs that is a good candidate to be permeable.

4. INTEGRATED INTERPRETATION

4.1 Preliminary completion test data analysis

For WK261, there are 10 interpreted feed zones in the preliminary analysis (Table 1, Figure 2). The major feed zone is #7 which exhibits anomalies for all data types and contains the pressure control point. Drilling losses were excluded from the analysis as multiple (14) lost circulation events in the last 300m of the borehole were all brief, do not correlate with other data and are more likely to be due to insufficient air during this period of aerated drilling.

For WK271 the interpretation of the completion test data is not as straightforward as for WK261 due to the presence of a large downflow entering the well around 1300 m resulting in a long isothermal section down to around 2050 m. This isothermal section is present at all injection rates and masks the temperature response which might be expected from any feed zones within this section.

For WK271 there are 7 interpreted feed zones in the preliminary analysis (Table 2, Figure 3). It is not possible to identify the major feed zone: while the PCP coincides with FZ #4 (spinner anomalies but not temperature due to masking), this may not be the major zone as the PCP is also approximately at the midpoint between the source of the downflow (FZ #1-3) and the end of the isothermal section (FZ #6).

Table 1: WK261 preliminary feed zone interpretation

		Data types – presence of anomalies				
Feed zone ID	**Depth range m**	**Temp. Grad. Inj.**	**Temp. Grad. Heat.**	**Spin**	**Spin ratio**	**PCP**
1	1150-1180	Y1 1150-1180	Y1 1150-1180	N	N	N
2	1280-1310	Y1 1280-1310	Y1 1280-1310	N	N	N
3	1390-1420	Y1 1390-1410	Y1 1390-1410	N	Y2 1400-1420	N
4	1450-1490	Y1 1450-1470	Y1 1450-1470	N	Y1 1470-1490	N
5	1560-1630	Y1 1560-1630	Y1 1560-1630	N	N	N
6	1670-1690	Y1 1670-1690	Y1 1670-1690	N	N	N
7 major	1810-1880	Y2 1810-1850	Y2 1810-1850	Y2 1800-1850	Y1 1820-1840	Y1 1850-1880
8	1890-1910	N	Y1 1890-1910	N	N	N
9	1980-2010	N	N	Y2 1980-2010	N	N
10	2050-2059	Y1 2040-2059	Y1 2040-2059	n/a	n/a	N

* Y1 (yellow) = yes, certain; Y2 (brown) = yes, uncertain; N (white) = no.

Table 2: WK271 preliminary feed zone interpretation

		Data types – presence of anomalies				
Feed zone ID	**Depth range mCHF**	**Temp. Grad. Inj.**	**Temp. Grad. Heat.**	**Spin**	**Spin ratio**	**PCP**
1	1230-1255	Y1 1230-1255	Y1 1230-1255	N	N	N
2	1265-1290	Y1 1265-1290	Y1 1265-1290	N	Y1 1260-1350	N
3	1305-1330	Y1 1305-1330	Y2 1305-1330	N		N
4	1610-1730	N	N	Y2 1680-1730	Y1 1650-1720	Y2 1610-1670
5	1910-1980	Y1 1910-2180	Y1 1910-2180	Y2 1910-2050	Y1 1910-1980	N
6	2030-2090				Y1 2030-2090	N
7	2130-2150			Y2 2130-2150	Y2 2130-2150	N

* Y1 (yellow) = yes, certain; Y2 (brown) = yes, uncertain; N (white) = no.

4.2 Borehole image log analysis

In WK261, 699 fractures were identified, and are dominantly of low acoustic amplitude (Table 3), of which 97 are also observed on the travel-time image. In WK271, significantly more (2299) fractures were identified on the resistivity image log, and are dominantly of low resistivity. Eighty-one of these are of low resistivity fractures and display a high resistivity halo. Excluding fractures of high acoustic amplitude in WK261, and those of high resistivity in WK271, which are most likely infilled with minerals, yields 698 potentially permeable fractures in borehole WK261, and 2143 in borehole WK271.

In WK261, fracture thickness measured perpendicular to the fracture walls varies is <895 mm, with 75% of fractures <12.4 mm. In WK271, fracture thickness is <169 mm, with 75% of fractures <6.2 mm. In both cases, the thickest fractures likely form a fractured zone rather than individual structures. The ability of resistivity image logs to detect thinner fractures than acoustic image logs relates to the different types of signals acquired, resistivity image logs being more susceptible to fine variations of mineral properties, while acoustic image logs are more susceptible to the borehole roughness as caused by large open fractures (Davatzes and Hickman, 2011).

Table 3: Length of imaged interval and number of fracture interpreted on each image log. Fracture morphology: HA: high acoustic amplitude; LA: low acoustic amplitude; LAT: low acoustic amplitude and visible on the travel-time image; HR: high-resistivity; LR: low resistivity; H: low resistivity with high resistivity halo.

Borehole	Length of imaged interval (m)	Number of fractures on image logs
WK261 (acoustic)	902	699 (HA: 1; LA:601; LAT: 97)
WK271 (resistivity)	955	2299 (HR: 156; LR: 2062; H: 81)

4.3 Integrated analysis of permeable zones in WK261 with acoustic image log interpretation

The cumulative fracture thickness displays large steps coinciding with nearly all permeable zones initially interpreted from completion tests, despite the datasets being independent (Figure 2d, in log-linear scale). There is a large contribution of these steps from the thickest fractures (as displayed by the cumulative fracture thickness for the 25% thickest fractures), rather than by numerous closely-spaced thin fractures. These thickest fractures are dominantly of low acoustic amplitude and seen on the travel time image. The location and extent of each feed zone was thus confirmed by the combination of both datasets. Although it is not possible to rule out a partial contribution to permeability by matrix, all feed zones have some fracture permeability.

The major feed zone (FZ#7), initially 70-m thick can be directly linked to two specific, thick fractures seen on the travel-time image, and other thinner fractures of the same morphology. Similarly, the sharp temperature increase observed on temperature logs during injection and heat-up in FZ#4 can be related to a single thick fracture seen on the travel time image.

Feed zones which do not display any significant thick fractures visible on travel-time image are minor (feed zones 1 and 8). Permeability may be dominantly controlled by the matrix (tuff lithology) rather than by fractures.

Interpretation of image logs provide an added, independent line of evidence to confirm the presence and extent of permeable zones controlled by fractures. Due to the high quality of the completion test data and therefore the preliminary interpretation, the feed zones have in this case not changed much by integrating with the image log interpretation data. However, the feed zone interpretation is more robust.

4.4 Integrated analysis of permeable zones in WK271 with resistivity image log interpretation

In WK271, it is more difficult to interpret the completion test data due to the presence of a large downflow, masking any potential temperature anomalies. This shortcoming in the completion test data creates an ideal circumstance for the fracture dataset to make a significant contribution to the refinement of the location of feed zones.

As discussed in Section 4.1 the major feed zone is not clear from completion test data alone, however with fracture data it can be confidently interpreted as FZ#4. There is a good correlation between the occurrence of fractures of low resistivity displaying a high resistivity halo and feed zones delineated independently from completion tests. FZ#4 contains 43% of all fractures with halo identified in the borehols, though this interval covers only 13% of the total imaged borehole length. The 3D geological model, based on stratigraphic offsets and detailed LiDAR surface fault mapping (Villamor et al., 2015), indicates that the Kaiapo Fault intersects WK271 near this feed zone (precise depth unconstrained due to the similar borehole trend and fault dip direction). Fractures with haloes may thus be related to the damage zone of the Kaiapo fault. The other fractures with haloes are dominantly located in feed zones 5 and 6. The correlation between thick fractures and feed zones identified in WK271 resistivity image log is not as clear as in WK261 acoustic image log.

FZ#1 and FZ#6 occur at the interface between lithologies, which suggests a lithological control on permeability. The image log does not extend to the bottom of the borehole, so the source of permeabiity in FZ#7 is not clear.

5. DISCUSSION

5.1 Efficiency of the process

Using this integrated process, the discussion of the extent and fracture/matrix components of permeable zones takes a relatively short time compared to the prior interpretation of completion tests and image logs. Within this short time, discussions add a greater degree of certainty to subsequent interpretations, including the extent/location of feed zones, identification of the major feed zone(s) in a well, with a compromised completion test dataset and indications of the fracture/matrix contribution.

Based on the apparent correlation between fracture type/thickness and permeability indicators in acoustic image logs, an additional step not undertaken in this study would consist of extracting very minor zones of permeability, such as in FZ#5 in WK261. In this FZ, individual thick fractures can be associated with specific temperature gradient changes, which qualifies them as permeable. While such detailed analysis of individual permeable fractures is not critical for reservoir management purposes, it is the base for fundamental research studies aiming at understanding the tectonic settings and interactions with fluid circulations in a given stress state (Barton et al., 1995). In turn, these structural and geomechanical studies help to site wells which will have an increased success of finding high permeability.

5.2 What does a permeable fracture look like?

Figure 6a displays fractures located in the major FZ# 7 in borehole WK261. Two fractures, respectively 0.5 and 0.9m-thick, appear clearly on the travel-time image which indicates that the borehole wall is rough, likely caused by spalling from the borehole wall at the intersection between these open fractures and the borehole wall.

Similar features observed in WK261 (Figures 6b-c) are not associated with either a temperature gradient change, or a clear spinner drop. At 1910-1920 m ((Figures 6b), the spalling from the borehole wall is so intense that it was difficult to identify individual fractures, and this zone was suggested by the geologist as a good contender for fracture permeability. This confirms that acoustic image logs alone cannot identify permeable fractures, but rather identifies potential permeable fractures which can be validated (or not) by completion tests.

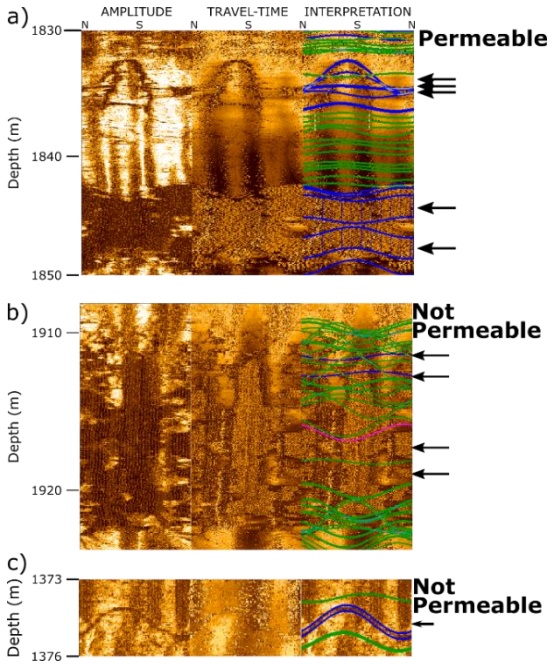

Figure 6: WK261 acoustic image log: permeable and non-permeable fractures of low acoustic fractures and visible on the travel-time image (arrows). a) major FZ#7; b) spalling from the borehole wall in a non-permeable zone; c) non-permeable zone. Statically normalized images with from left to right: amplitude image, travel-time image and travel-time with fracture interpretation.

The contribution to permeability of the numerous fractures <30 mm-thick located in feed zones (such as in Figure 6a) is unclear. In addition, 66% of fractures detected on the WK261 image log are not located in any feed zone. These fractures may be infilled with low acoustic amplitude material such as clay, or lack sufficient connectivity to the permeable fracture system (Kissling and Massiot, this volume). While not critical to the reservoir management, non-permeable fractures are very useful to evaluate the tectonic settings in relationships to the *in-situ* stress (McNamara et al., 2015). These fractures which were not permeable at the time of the completion test may also be reactivated by subsequent natural seismicity or borehole stimulation, and thus may provide additional permeability at a later stage.

Figure 7a presents thick low-resistivity fractures in borehole WK271, some with high resistivity haloes, located within major FZ#4. Similar features are observed in zones without any permeability indicators (Figure 7b). In this case, hydrothermal mineralisation may have filled-in the fracture, preventing fluid flow. Current investigation of the slip tendency of these fractures within the *in-situ* stress field are ongoing to investigate the possible nature of these fractures.

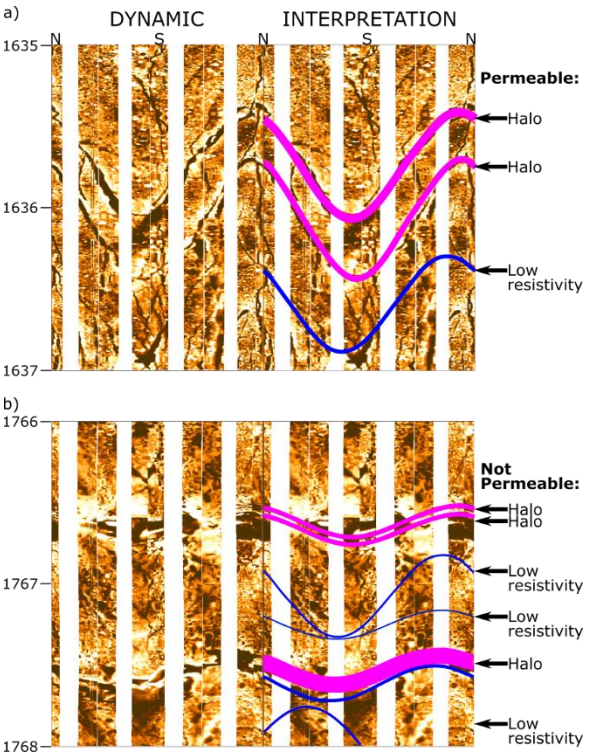

Figure 7: Dynamically normalized WK271 resistivity image log of fractures with haloes in a) a permeable zone and b) a non-permeable zone.

5.3 Evidence of matrix-controlled permeability

FZ#6 in WK271 is located at the interface between a partially welded ignimbrite and a rhyolite lava as defined from cuttings observations. The resistivity image log displays a zone of low resistivity (Figure 8). In this case, it is likely that permeability occurs at the interface itself, associated with one or several of these contributions:

- The interface itself serving as a fluid pathway
- The brecciated carapace of the rhyolite
- Increased fracturing at the base of the partially welded ignimbrite potentially caused by a local increase in welding indiscernible from cuttings (Smyth and Sharp, 2006)

Fractures with haloes are also observed near this interface (Figure 3) which could be caused by increased water-rock interactions. Further textural analysis of the resistivity image log is ongoing to evaluate lithological controls on fracturing and permeability.

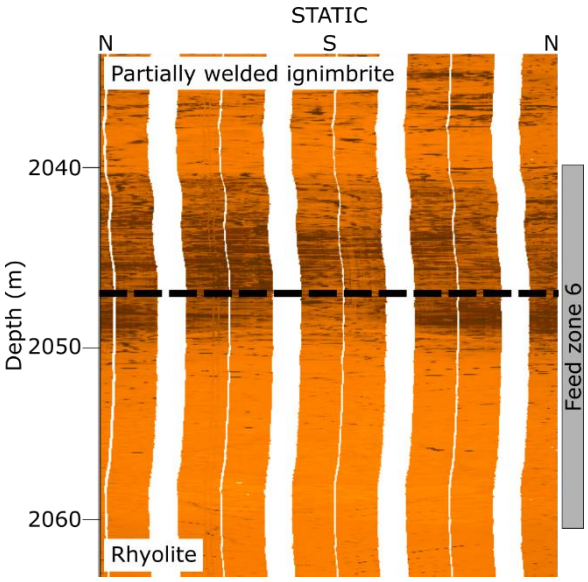

Figure 8: WK271, lithological control on permeability: FZ#6 (grey square), at the interface (dashed line) between a partially welded ignimbrite and a rhyolite (as defined from cuttings), coincides with a pervasive low-resistivity zone (dark grey). Statically normalized resistivity image.

5.4 Strategy to identify potentially permeable fractures in acoustic and resistivity image logs

Permeable fractures in borehole image logs in the two boreholes used in this study have different characteristics. In acoustic image logs, thick (>15-20 mm) fractures of low acoustic amplitude and visible on the travel-time image are good contenders to be permeable. Similar observations have been made in nearby boreholes WK264 and WK266 (unpublished), as well as previously reported by McLean and McNamara (2011) in three other boreholes in the Wairakei Geothermal Field. So, for the Wairakei Geothermal Field, rapid interpretation of potential fracture-dominated permeable zones can be attempted using acoustic image logs, and then integrated with a preliminary assessment of permeable zones from completion test data. Further in-depth analysis of both datasets can then be made at a later stage.

In a similar study of the andesitic formations hosting the Rotokawa reservoir, a correlation between such thick low acoustic fractures seen on the travel-time image and permeable zones was demonstrated for some of the permeable zones (McNamara et al., 2015), but not as systematically as at Wairakei. So, morphological characteristics of good contenders for being permeable needs to be tested for each geothermal field, or at least each reservoir rock type.

Based on the first resistivity image log acquired in the Wairakei Geothermal Field (WK271), low resistivity

fractures with high resistivity haloes seem to correlate with the major feed zone (FZ#4) also coinciding with a modelled fault zone, and with minor feed zones #5 and #6, making them good contenders for rapid identification of potential permeable fractures. Halwa et al. (2013) interpreted similar features observed in the nearby Ngatamariki Geothermal Field as an indicator of fractures filled with highly conductive minerals, such as pyrite or magnetite. In borehole WK271, the high conductivity of these permeable fractures with haloes may be related to the presence of fluids in the fracture, or to actual changes of mineralogy near the fracture walls caused by intense water/rock interactions. Further resistivity log acquisition will undoubtedly help with defining which fracture morphology is likely to be permeable. Areas of pervasive low resistivity as presented on Figure 7 may also provide guidance for matrix-controlled permeability.

6. CONCLUSION

For the Wairakei Geothermal Field, thick fractures with low acoustic amplitude also visible on the travel time on acoustic image logs are good contenders for being permeable. Based on the first resistivity image log acquired at Wairakei, low resistivity fractures with high resistivity haloes are good contenders for being permeable, and in this case occur predominantly in the vicinity of a reservoir-scale fault. To conclusively identify whether these fractures are actually permeable requires independent analysis of completion test data, where both datasets inform each other. Discussions between the reservoir engineer and geologist enhances the value of these datasets, providing a significant dimension of robustness to interpretations and work within the two disciplines, and ultimately improved reservoir models and field management. The individualisation of permeable fractures in image logs is also crucial to further understand tectonic and water-rock interaction processes in high-temperature geothermal systems.

ACKNOWLEDGEMENTS

This study is part of a contribution from GNS Science's *Geothermal Resources of New Zealand* and *New Zealand Geothermal Future* research programmes, funding of which was provided by the Government of New Zealand. We thank Contact Energy Ltd for the provision and permission to publish well data. The authors acknowledge support of this work by Haliburton Software and Services, a Haliburton Company, through the use of Recall™ Borehole software.

REFERENCES

Barton, C. A., Zoback, M. D., & Moos, D. (1995). Fluid flow along potentially active faults in crystalline rock. Geology, 23(8), 683–686.

Davatzes, N. C., and S. H. Hickman (2010), Stress, fracture, and fluid-flow analysis using acoustic and electrical image logs in hot fractured granites of the Coso Geothermal Field, California, U.S.A., in *Dipmeter and borehole image log technology: AAPG Memoir 92, edited by M. Poppelreiter, C. Garcia-Carballido, and M. Kraaijveld*, pp.259–293, *AAPG Special Volumes*, doi:10.1306/13181288M923134.

Grant, M. A., & Bixley, P. F. (2011). Geothermal Reservoir Engineering (2nd ed.). Burlington, USA: Academic Press.

Halwa, L., Wallis, I. C., & Lozada, G. T. (2013). Geological analysis of the volcanic subsurface using borehole resistivity images in the Ngatamariki Geothermal Field, New Zealand. *New Zealand Geothermal Workshop 2013 Proceedings*.

Kissiling, W. and Massiot, C. (submitted): Geometrical modelling of fracture networks in an andesite-hosted geothermal reservoir. *This volume.*

Lofts, J.C., and Bourke L.T. (1999) The recognition of artefacts from acoustic and resistivity borehole imaging devices. *Geological Society of London, Special Publication Vol 159:59-76.*

Massiot, C., McNamara, D. D., & Lewis, B. (2013). Interpretive review of the acoustic borehole image logs acquired to date in the Wairakei-Tauhara Geothermal Field. *GNS Science report 2013/04.* 26 p.

Massiot, C., McNamara, D. D., & Lewis, B. (2015). Processing and analysis of high temperature geothermal acoustic borehole image logs in the Taupo Volcanic Zone, New Zealand. *Geothermics*, 53, 190–201. Doi: 10.1016/j.geothermics.2014.05.010

Massiot, C.; Nicol, A.; McNamara, D.D.; Townend, J. (2017). Evidence for tectonic, lithologic and thermal controls on fracture system geometries in an andesitic high-temperature geothermal field. *Journal of Geophysical Research* (122).

McLean, K., & McNamara, D. (2011).; Fractures interpreted from acoustic formation imaging technology: correlation to permeability, *Proceedings 36th Workshop on Geothermal Reservoir Engineering, Stanford.*

McNamara, D. D., & Massiot, C. (2016). Geothermal Structural Geology in New Zealand: innovative characterisation and micro-analytical techniques. *Proceedings 38th New Zealand Geothermal Workshop.*

Milloy, S., Mclean, K., & Mcnamara, D. D. (2015). Comparing Borehole Televiewer Logs with Continuous Core: An Example from New Zealand. *World Geothermal Congress Proceedings*.

Siega, C., Grant, M., Bixley, P., & Mannington, W. (2014). Quantifying the Effect of Temperature on Well Injectivity. *Proceedings of the 36th New Zealand Geothermal Workshop*, 24-26 November, Auckland, New Zealand.

Smyth, R. C., & Sharp, J. M. (2006). The hydrology of tuffs. In Tuffs - Their Properties, Uses, Hydrology, and Resources (pp. 91–111). *Geological Society of America*. doi: 10.1130/SPE408

Villamor, P., Clark, K., Watson, M., Rosenberg, M. D., Lukovic, B., Ries, W., & González, Á. (2015). New Zealand Geothermal Power Plants as Critical Facilities: an Active Fault Avoidance Study in the Wairakei Geothermal Field, New Zealand. World Geothermal Congress 2015, 19–25.